Role of Mechanical van der Waals Coupling in the *G*-band Splitting of Individual Multi-Wall Carbon Nanotubes

Marina V. Avramenko[1,4], Matti J. Hokkanen[2,†], Yuri Slabodyan[1], Markus Ahlskog[2], Dmitry I. Levshov[1,3,]*

[1] Faculty of Physics, Southern Federal University, 5 Zorge Street, Rostov-on-Don 344090, Russia

[2] Department of Physics and Nanoscience Center, University of Jyvaskyla, Jyvaskyla, FI-40014, Finland

[3] Physics Department, University of Antwerp, Universiteitsplein 1, B-2610 Antwerp, Belgium

ABSTRACT

Characterization of multi-walled carbon nanotubes (MWCNT) by Raman spectroscopy is challenging due to their structural complexity, inhomogeneity and complicated interlayer van der Waals (vdW) interactions. These latter effects can be however well investigated in individual MWCNTs, prepared by the on-chip purification of arc-discharge (AD) MWCNT powder, combining atomic force microscopy, polarized Raman imaging and spectroscopy. In this work, we reveal the inhomogeneity of the Raman signal from individual AD-MWCNTs and attribute it to the extraction of inner layers during the sonication stage of the dispersion procedure. We report the splitting of

Raman-active *G*-band, describing it in terms of the variation of inter-layer mechanical vdW coupling as a function of diameter and interlayer distance in the probed AD-MWCNTs. Finally, we present a practical method for investigating the polarization behavior of MWCNTs with a non-uniform Raman response based on Raman mapping and advanced data fitting. Our work gives additional insights into the characterization of structurally non-uniform MWCNTs and allows distinguishing between these MWCNTs and 1D moiré crystals based on collapsed SWCNTs or studying telescopic 1D vdW heterostructures with Raman spectroscopy.

INTRODUCTION

Multi-wall carbon nanotubes (MWCNT) represent a broad class of one-dimensional carbon materials, existing in several distinct forms, such as coaxially stacked cylindrical[1] or polygonized[2] shells, scrolls[3], or herringbone structures[4]. MWCNTs are mechanically robust due to strong sp^2 carbon-carbon bonds and have a large outer surface area and broad hollow inner space, accessible for molecular grafting and encapsulation, respectively. The MWCNT electronic and optical properties are defined by those of the individual walls, which can be metallic or semiconducting with a variable band gap depending on the diameter and roll-up (chiral) angle[5]. However, they generally act as metals due to averaged responses from multiple metallic and semiconducting layers. In addition, the electronic band structure of MWCNTs is modulated by the van der Waals (vdW) electronic coupling[6] and moiré interference[7], resulting in the appearance of flat bands or pseudogaps[8].

Owing to these remarkable properties and low production costs, MWCNTs find multiple applications in composite materials[9], biotechnology[10,11] and electronics[12]. The high surface area of MWCNTs is used to support other molecules, *e.g.*, the molecular catalysts for photoelectrochemical cells[13] or single atomic catalysts[14]. The inner channels of MWCNTs are actively exploited as the nanoscale chemical labs to grow 1D materials[15] or to probe the fundamental properties of encapsulated

materials[16]. Finally, MWCNTs are still widely used for fundamental studies, *e.g.*, to determine the angle-dependent conductance of nanotubes[17] or to investigate the adsorption of DNA on the MWCNT surface[18].

The structural characterization of MWCNTs is an essential step for many of these applied and fundamental studies. One of the most powerful techniques in this regard is resonant Raman spectroscopy (RRS), which was shown to provide extensive structural information for single-wall carbon nanotubes (SWCNT)[19,20]. However, applying the same characterization principles to MWCNTs is challenging due to their structural complexity and inhomogeneity or complicated inter-layer vdW interactions[4]. So far, RRS on MWCNTs has been limited to estimating the defect density (ratio of I_D/I_G or I_D/I_{2D}), measuring inner layer diameters from radial breathing mode frequencies, doping state through the shift of *G*-modes, or verifying the encapsulation or functionalization of molecules (see review in Ref. [4]).

In the present paper, we probe the role of mechanical vdW coupling and structural inhomogeneity for characterization of individual MWCNTs by combining Atomic Force Microscopy (AFM), polarized Raman imaging and RRS measurements. The pure individual MWCNTs were obtained from arc-discharge (AD) synthesized MWCNTs using the on-chip purification method[21]. We reveal the inhomogeneity of the Raman signal from AD-MWCNTs and ascribe it to the inner layers extraction or damage during the sonication step of the dispersion procedure. We report the splitting of Raman-active *G*-band in isolated individual MWCNTs and describe it in terms of the varying inter-layer mechanical vdW coupling being the function of diameter and interlayer distance. Finally, we present a practical method for probing the polarization behavior of MWCNTs with a non-uniform Raman response based on Raman mapping and advanced data fitting, which allows identifying the antenna effect.

METHODS

Materials. AD-MWCNTs were obtained from MER Corp., Sigma-Aldrich or collaborating group in Japan (A. Koshio, Iijimatubes). A powder of catalyst-free MWCNT material (containing also amorphous carbon particles) was dispersed in 1,2-dichloroethane, and the resultant suspension was sonicated for c. 10 minutes. This dispersion was deposited via spin coating on the Si/SiO_2 substrates. The Si substrates had prefabricated marker structures, which enabled localization with AFM of individual and clean cases among the randomly dispersed MWCNTs.

Atomic Force Microscopy. AD-MWCNTs were structurally characterized using a Bruker Dimension ICON platform used in conventional tapping mode with two types of Si probes bought from μMasch: HQ:NSC14 (f = 160 kHz, k = 5 N/m) and HQ:NSC15 (f = 325 kHz, k = 40 N/m).

Raman spectroscopy. Resonant Raman spectra from individual MWCNTs, localized on the substrate with respect to the marker structures, were excited with an Ar ion laser (514 nm / 2.41 eV) and recorded using a single monochromator Renishaw InVia Reflex spectrometer, equipped with an edge filter (cut-off frequency at 50 cm^{-1}) and Si CCD detector. All experiments were performed in the backscattering geometry under ambient conditions. A 100x microscope objective was used to focus the laser beam and collect the scattered light. The laser spot had a diameter of ~1 μm at the sample with a power density of ~106 W/cm^2. The Raman spectra of MWCNTs were registered in three spectral regions: RBM, *D* and *G*, and 2*D* bands. For the polarized measurements, the sample with MWCNTs was placed on the rotation stage and rotated manually with a step of 10°. A fixed polarizer was used to analyze the scattered light polarized parallel to the incident-light polarization (VV configuration). To obtain the VH signal (incident and scattered light polarized perpendicular to each other), we rotated the scattered light polarization by a half-wave plate, keeping the same scattered-light polarization direction in the grating and the CCD.

RESULTS AND DISCUSSION

Non-uniform Raman response from individual MWCNTs. We investigated six samples with AD-MWCNTs deposited on the Si/SiO_2 substrates and purified by the liquid immersion technique from residual amorphous carbon (see Supporting Information (SI) Section S1)[21]. Using the AFM, we located overall 26 isolated individual AD-MWCNTs relative to the prefabricated markers (Fig. 1a-b and SI Section S2; individual SWCNTs and SWCNT bundles were avoided). These MWCNTs had outer diameters in the range 3.9 − 17.5 nm and lengths from 1 to 4 μm, as summarized in Table S1 (SI Section S3). We found that 18 of 26 MWCNTs were in resonance when probed with the 514 nm laser excitation wavelength. The radial breathing-like modes (RBLM) were not detected for any of the investigated MWCNTs in contrast to previous studies on macroscopic ensembles of AD-MWCNTs by SERS[22], which suggest that we probed mainly large-diameter intermediate or outer layers (see discussion in SI Section S4).

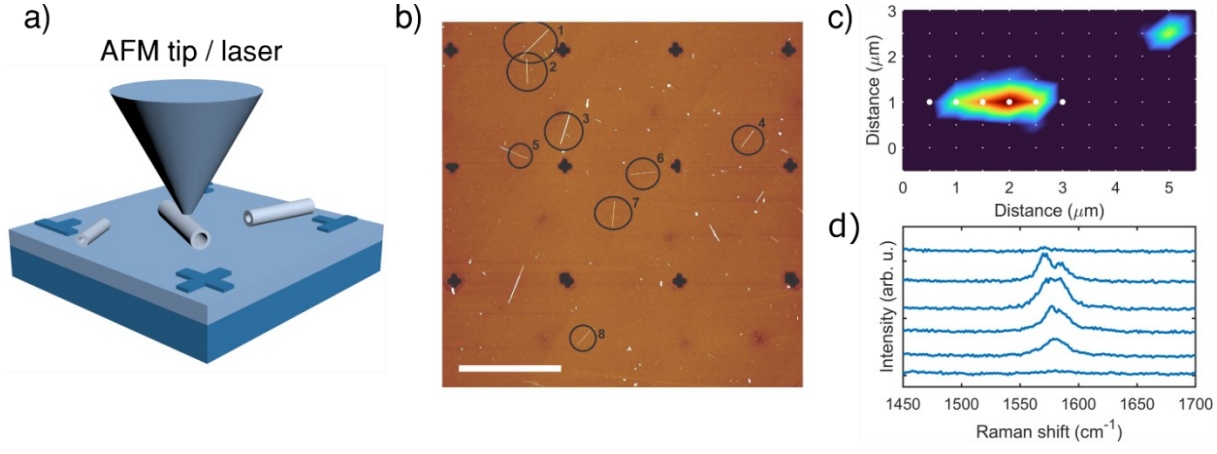

Figure 1. (a) Schematics of the experimental approach combining AFM and RRS on the same individual AD-MWCNTs using the prefabricated markers for localization. (b) AFM image showing a substrate with 8 studied AD-MWCNTs (marked by circles). The white scale bar is 7 μm. (c) *G*-band Raman map of a representative AD-MWCNT (number 6 in (b)) obtained by integrating the

Raman intensities from 1510 to 1640 cm^{-1}. Small white dots indicate the RRS measurement coordinates. (d) The *G*-band Raman spectra of the AD-MWCNT extracted from the map in (c) at the positions shown by large white dots, highlighting the non-uniform Raman response.

We note that most of the studied AD-MWCNTs had a non-uniform distribution of the Raman signal along their lengths, as shown by the *G*-band Raman intensity map in Fig. 1c. The map was obtained from Raman spectra measured around a representative AD-MWCNT with a step of 0.5 μm by integrating Raman intensities from 1510 to 1640 cm^{-1}. Small white points in Fig. 1c represent the actual measurement locations at the substrate, while the large white dots on the MWCNT correspond to the Raman spectra shown in Fig. 1d (top-to-bottom spectrum order corresponds to the right-to-left order of the dots along the MWCNT in Fig. 1c). The *G*-band spectra clearly vary along the length, which required us to use Raman imaging systematically for the complete structural characterization of AD-MWCNTs.

We tentatively assign the non-uniformity of the Raman signal to the existence of structural modifications along MWCNTs, *e.g.*, the sudden termination of specific layers leading to the so-called telescopic structure. The latter was observed on similar AD-MWCNTs in our recent high-resolution scanning tunneling microscopy (STM) and AFM studies[23]. Such structural inhomogeneities may appear during the post-synthesis processing, *e.g.*, during sonication widely used for solubilization of CNTs in surfactants[24]. Previously, high-resolution TEM[25] (HRTEM) and optical spectroscopy[26] studies reported that the sonication leads to the extraction of inner layers from double-wall CNTs (DWCNT), the simplest case of MWCNTs. In our case, it can lead to the complete or partial sliding of inner shells from outer MWCNT layers creating a telescopic geometry or to the formation of defects. However, the I_D/I_G ratio for most of the studied AD-MWCNTs was less than 0.05 (see Ref.

[23]), which is substantially lower than the one observed for CVD-grown MWCNTs in the literature (I_D/I_G from 0.5 to 1)[27] and indicates that AD-MWCNTs conserve their high crystalline quality[4].

G-band splitting in individual AD-MWCNTs. Another important feature evident from Figure 1d is the splitting of the *G*-band, *i.e.*, the appearance of multiple phonon peaks in the high-frequency spectral range between 1550 and 1610 cm^{-1}. Such behavior was previously reported in the surface-enhanced Raman studies[22] or gate-dependent Raman measurements[28] on AD-MWCNTs. The latter work tentatively assigned the lower-frequency *G*-band peaks to the inner-most shells since they were not sensitive to gate voltage change, presumably due to the screening by outer layers. We note that this *G*-band splitting is systematically found in most of the studied AD-MWCNTs, as illustrated by their unpolarized Raman spectra in Figure 2a.

The peculiar *G*-band structure in AD-MWCNTs contrasts with the usual one-peak *G*-band spectrum of graphene and highly ordered pyrolitic graphite (HOPG), where it consists of two degenerate E_{2g} phonons with the same frequency (see the topmost spectrum in Figure 2a)[29]. When the graphene is rolled into a nanotube, the degeneracy is lifted by the curvature and quantum confinement effects[30], resulting in six new *G*-modes in a chiral SWCNT ($2A_1+2E_1+2E_2$) or three modes ($A_{1g} + E_{1g} + E_{2g}$) in an achiral SWCNT[31]. However, the strong depolarization (antenna) effect in SWCNTs severely attenuates light absorption and emission in the direction perpendicular to the nanotube axis, leading to the complete suppression of E_1 and E_2 modes[32]. It means in practice that only two A_1-symmetry lines can be observed in an isolated free-standing SWCNT with frequencies depending on the diameter[20,30]. These dependencies are illustrated by solid blue and orange lines in Figure 2c, corresponding to the transverse optical (TO or $G-$) and longitudinal optical (LO or $G+$) modes of semiconducting SWCNTs, respectively.

When two or more SWCNTs are combined into a MWCNT, the total *G*-band becomes composed of a sum of the layers' *G*-modes[33,34], affected to some extent by the mechanical vdW interlayer coupling. We previously established on the example of individual semiconducting DWCNTs that the vdW coupling could shift the inner and outer layer *G*-modes apart compared to their frequencies in isolated SWCNTs[35,36]. The *G*-band shift was explained by two effects: variation of carbon-carbon bond length upon structural relaxation or interaction between the layers after relaxation[35]. The former depends strongly on the distance between the layers Δr and layer diameter d. For instance, in a set of semiconducting DWCNTs with a fixed inner layer diameter d = 2.2 nm, the $G-$ line shifts relative to its frequency in a SWCNT by the value varying from +12.5 cm^{-1} to −20 cm^{-1}, when the interlayer distance Δr changes from 0.32 nm to 0.38 nm, respectively[35]. The zero shift corresponds to $\Delta r \approx$ 0.335 nm, *i.e.*, the equilibrium interlayer distance in the HOPG. The shifted *G*-band spectra in DWCNTs resemble the observed splitting in AD-MWCNTs.

We therefore investigate the role of vdW mechanical coupling in the *G*-band splitting of AD-MWCNTs. Since this coupling was shown to depend on the interlayer distance Δr and layer diameter d[35], we statistically analyze the correlation between these parameters in different MWCNTs. We review 335 DWCNTs and 41 distinct pairs of layers in 15 MWCNTs unambiguously characterized by electron diffraction (ED) or HRTEM from several tens of papers (for a full reference list of DWCNTs, see Refs. [37,38]; MWCNT data were taken from Refs. [39–43]). These data are also complemented by HRTEM studies by Kiang *et al.*[44]. The MWCNT interlayer distances are plotted as the function of outer layer diameter in Figure 2b with gray symbols. They scatter significantly between 0.3 and 0.5 nm for layers with d < 5 nm but tend to about 0.344 nm for d > 10 nm. This scattering can be tentatively assigned to the chirality dependence of the minimum energy configurations of MWCNTs as reported in Ref. [45]. In short, among all geometrically possible

configurations of layers of a MWCNT, some have the minimum energy due to the vdW interaction. The energy difference between this optimum configuration and other possible configurations is high at large layer diameters but becomes negligible at small diameters. The latter implies that a higher number of structural configurations can grow with almost equal probability leading to the large scattering of the data points. In contrast, large diameter nanotubes tend to grow in the minimum energy states, characterized by similar chiral angles of the adjacent layers and interlayer distances close to the one in graphite[45].

Previously, Kiang *et al.*[44] proposed an empirical relation predicting the interlayer distance in MWCNTs to decrease exponentially with increasing the diameter (solid blue line in Figure 2b). We note that this prediction contrasts with the observed large data spread below 5 nm, which can be explained by the limited number of observations available in Kiang's work.

To account for data variation, we statistically analyzed the distribution of points among different values of diameters and interlayer distances (see the bivariate histogram in Figure S5). We found that majority of the data are clustered in a region whose top and bottom bounds can be approximated by the functions represented by dashed red curves in Figure 2b. These curves were obtained through a linear-least square regression (SI Section S5) and allow predicting the possible extreme values of interlayer distance Δr for a given layer diameter d of a MWCNT.

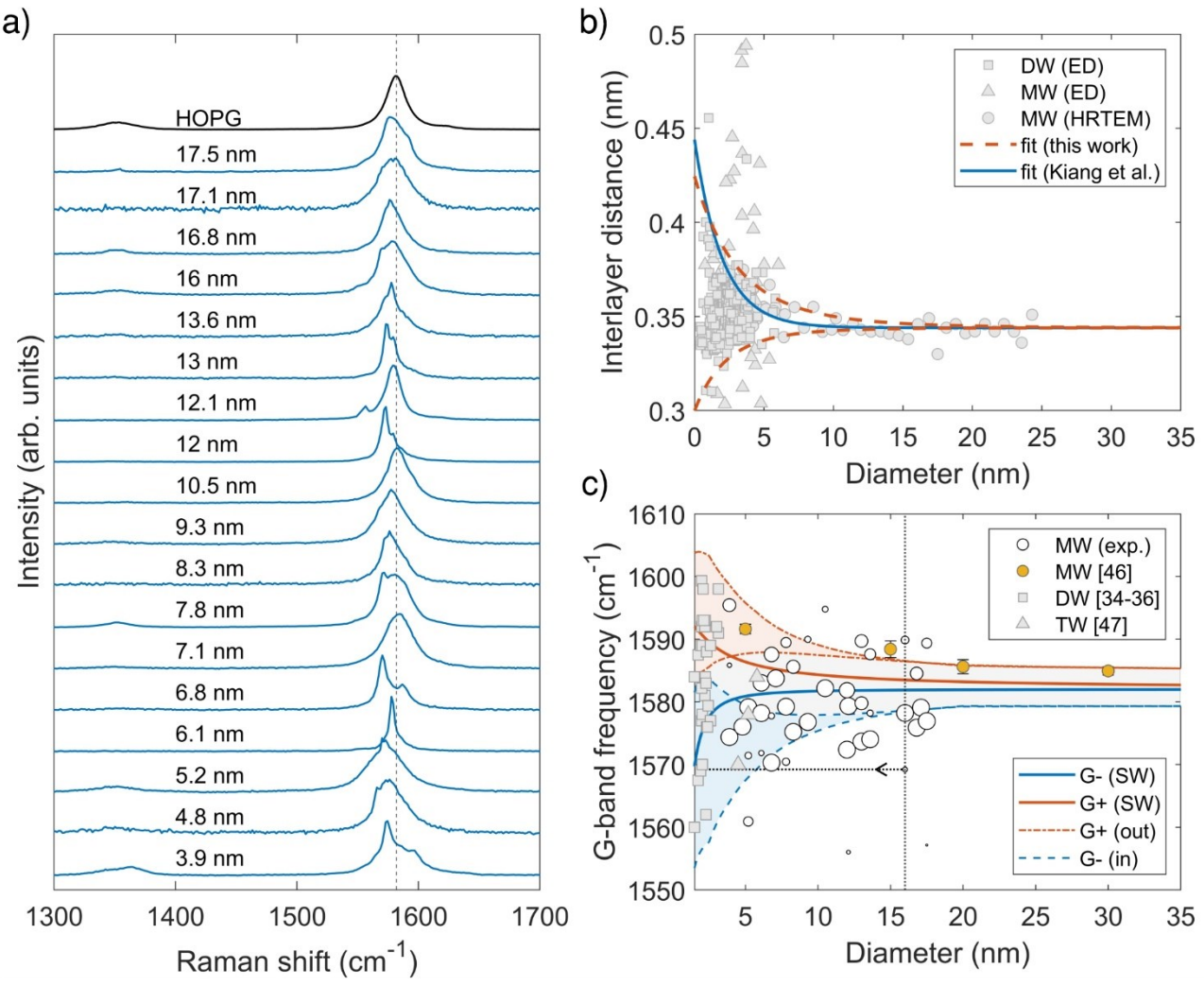

Figure 2. Raman spectroscopy of individual AD-MWCNTs: (a) *G*-band range of unpolarized Raman spectra of investigated AD-MWCNTs and HOPG. The labels show the outer layer diameter obtained from AFM measurements. (b) Dependence of interlayer distance Δr in DWCNTs[37,38] and MWCNTs[39–43] on the diameter d established by ED and HRTEM measurements. Solid blue line represents the empirical relation obtained by Kiang *et al.*[44], while dashed red curves designate the upper and lower bounds of $\Delta r = f(d)$ dependence estimated in this work based on the highest data point concentration. (c) Dependence of *G*-band frequency in MWCNTs on the layer diameter d. Open circles correspond to the fitted *G*-band frequencies from (a) plotted as a function of the outer tube diameter. Filled orange circles represent MWCNT data from Nii *et al.*[46], while gray squares and

triangles stand for the DWCNT[34–36] and TWCNT[47] data, respectively. Solid blue and orange lines illustrate the diameter dependence of the $G-$ and $G+$ mode frequencies in semiconducting SWCNTs[20,30], respectively. The calculated deviation in the $G-$ frequency of the inner layer and $G+$ frequency of the outer layer due to the large spread of Δr values in MWCNTs shown in (b) are represented by the dashed blue and dashed-dotted orange curves, respectively. The dotted horizontal line with an arrow originating from one of the open circles indicates that the G-mode corresponds to an inner layer and its true position should be within the blue area.

We then determined the *G*-band shift as a function of Δr and *d* by fitting the calculations of Popov *et al.*[35] for $G-$ and $G+$ phonons of inner DWCNT layers. The calculations are available for the diameter range 0.7 − 2.2 nm and contain the contributions from both relaxation- and interlayer interaction-induced effects in DWCNTs (Figure S6). To estimate the G-band shift in larger DWCNTs, we assume that the relaxation-induced effects become negligible with decreasing the layer curvature, and the total *G*-band shift is reduced to those determined by interlayer interactions. Popov *et al.* established that the latter changes in Bernal-stacked bilayer graphene from −4.87 to −0.67 cm^{-1} when its interlayer distance varies from 0.32 to 0.38 nm, respectively[35]. We assume that the transition between the small diameter (dominated by relaxation effect) and large diameter (dominated by interlayer interaction) regimes in a MWCNT happens continuously with increasing layer diameter from 2.2 to 20 nm. The latter diameter was tentatively established based on the combined Raman and X-ray studies of Nii *et al.*[46] on commercial MWCNTs (filled orange circles in Figure 2c), which showed that *G*-band frequencies decrease with the increase of MWCNT diameter and starting from d = 20 nm converge to almost a constant value at least up to d = 80 nm (Figure S7). As for the *G*-band in outer DWCNT layers, our experimental observations on individual DWCNTs[34] and calculations of Popov *et al.*[35] suggest that they exhibit an opposite behavior to that of the inner layers.

Therefore, as a first approximation, we assumed for them the same values of the shifts as for inner layers but with opposite signs.

We can now estimate the extreme *G*-band frequencies in the investigated range of MWCNT diameters resulting from vdW mechanical coupling. For this purpose, we first calculated the frequencies of *G*− and *G*+ phonons in SWCNTs using the empirical formulas established by Telg *et al.*[30] (solid orange and blue lines in Figure 2c, respectively). These data are then corrected for the extreme shift values $\Delta\omega_G$ estimated for inner and outer layers in DWCNTs. For the sake of clarity, we restrict ourselves to presenting the behavior of TO modes (*G*−) of inner layers and LO modes (*G*+) of outer layers, shown by the blue dashed and orange dash-dotted lines in Figure 2c, respectively. The filled blue and orange areas designate the range of variation of the *G*-band frequencies due to the large spread of interlayer distances Δr between the fitted top and bottom bounds in Figure 2b. Since the variation of Δr is decreased upon increasing the diameter, the variation of *G*-band frequencies is also reduced to a single frequency above $d = 15 - 20$ nm. We note that other Raman modes (*e.g.*, *G*+ of the inner layer) omitted for presentation clarity lie in the gray region between the blue and orange areas.

We now compare the calculations of the *G*-band shifts with the *G*-band behavior in MWCNTs index-identified by ED or HRTEM from the literature[34–36,47] and AD-MWCNTs from this work. The literature data consist of 45 measured *G*-mode frequencies in 15 DWCNTs[34–36] and 3 *G*-mode frequencies in a TWCNT[47] shown in Figure 2c by gray squares and triangles, respectively (see Table S2 in SI Section S6). Most of these experimental data points indeed differ from the expected *G*-band frequencies of SWCNTs (solid lines in Figure 2c), but lie exactly within the calculated *G*-band shifts and agree well with our model.

We also fitted the high-frequency Raman spectra of 18 AD-MWCNTs from Figure 2a with a set of Lorentzian functions as described in SI Section S7. In contrast to relatively easily interpretable Raman spectra of suspended DWCNTs and TWCNTs, the analysis of the Raman data from AD-MWCNTs on the substrate is more complicated. First, we do not know *a priori* which layer of the AD-MWCNT is in resonance, especially when RBM lines are not detected. Secondly, the only accessible structural parameter of the AD-MWCNT is the diameter of the outer layer estimated by AFM. This means that if we plot all fitted *G*-mode frequencies for a given AD-MWCNT versus the outer tube diameter, only one *G*-mode can be assigned to the outer tube, while others originating from the inner layers will be offset vertically.

We illustrate this by plotting the *G*-mode frequencies as a function of outer tube diameter in Figure 2c with gray dots. The size of the gray dots represents the relative intensity (peak height) in the given AD-MWCNT spectrum. In the whole experimental diameter range of 3.9 − 17.5 nm, most of the AD-MWCNTs have indeed at least one G-band frequency that lies within the calculated region of the G-band shifts and therefore should correspond to the outer tube. However, some points lie below or above the predicted ranges, *e.g.*, the one marked by the horizontal and vertical dotted lines in Figure 2c. This point can be interpreted as originating from an inner layer in resonance with the laser excitation energy but having a smaller diameter than the one determined by AFM. Therefore, the true position of the point should be at lower diameter values within the filled blue area, as indicated by the arrow in Figure 2c. This approach for analyzing MWCNT G-band spectra provides a way to roughly estimate the diameters of the layers corresponding to the shifted G-modes.

Finally, we discuss factors that can lead to the possible discrepancies between the calculations and the measured data. We note that in a MWCNT with three or more walls, an intermediate layer will be surrounded by two nanotubes. Therefore, the total effect of vdW coupling may differ from the

estimations based on the DWCNT model with only two interacting layers. Besides, we point out that according to Figure 2b, the interlayer distances in MWCNTs can sometimes attain values outside of the fitted top and bottom bounds. We treated these cases as outliers since they are rare according to the bivariate distribution (Figure S5). Still, they can lead to even greater *G*-band shifts than predicted in Figure 2c.

In addition, the described intrinsic *G*-band behavior in SWCNTs and MWCNTs can be affected by extrinsic factors, such as intentional doping[48,49] or accidental environment-induced[50,51] doping, applied strain[52] or temperature changes, *e.g.*, through laser-induced heating[53]. The inter-layer charge transfer was also reported to affect the MWCNT properties[54,55], but mainly in the case of interacting commensurate layers, which are statistically rare to observe in the experiment. The frequency shifts due to the laser-induced heating depend on the polarization of laser light relative to the MWCNT axis and were not observed in the experiment (see next section). The extrinsic strain should be minimal for a MWCNT with no bendings on the SiO_2 substrate. As for the doping, in any case, it would lead to the up-shift of *G*-band frequencies relative to the frequencies in undoped SWCNTs[48] and therefore can not explain the observed large downshifts of the *G*-band. The lower *G*-band frequencies may be also assigned to E_1 and E_2 phonons, activated by the symmetry rules breaking upon the interaction between the nanotube and the substrate[56]. However, this should mainly affect the outer-most layers of MWCNTs contacting the substrate and not the inner ones, which are shielded from environmental interactions[57]. Furthermore, previous surface-enhanced Raman studies[22] and gate-dependent Raman measurements[28] on AD-MWCNTs explained the low-frequency *G*-band peaks as originating from inner layers, which agrees with our conclusions and supports the interpretation of the *G*-band shifts as due to the mechanical vdW interaction.

Polarized Raman spectroscopy and imaging of structurally non-uniform MWCNTs. We also investigated the effect of structural non-uniformity on the polarization dependence of *G*-band in AD-MWCNTs. The schematic of our experimental set-up and the geometry of the polarized measurements are shown in Figure 3a. We note that the inhomogeneity of the Raman response (Fig. 1c-d) poses a significant challenge for polarized measurements, as it was difficult to locate the same spot on the MWCNT upon rotation of the sample. Therefore, we systematically measured full Raman maps with steps of 0.5 μm in VV and VH configurations (Fig. 3b) around the approximated position of the MWCNTs relative to prefabricated markers as a function of angle θ. The Raman spectra were corrected for the power variation using the integrated intensity of silicon peak at ~950 cm^{-1} (the polarization dependence of the Si peak intensity was also accounted for).

The measured dependence of the *G*-band on the light polarization direction for VV and VH configurations is visualized in Figure 3c (left and right panels, respectively) for a selected MWCNT. For presentation clarity, we plot only MWCNT spectra with the maximum *G*-band signal in the Raman map at the given θ angle (*e.g.*, the brightest point in Figure 3b). To describe the polarization dependence quantitatively, we selected all points with a non-zero *G*-band signal around the MWCNT position. For example, for $\theta = 140°$ they are shown with open white circles in Figure 3b. In this way, we obtained about 200 *G*-band Raman spectra combining both VV and VH configurations and all θ angles. We then performed their simultaneous fit by using a sum of Lorentzian functions and sharing peak parameters between all the spectra. This fitting approach was adapted for the analysis of polarized Raman mapping from the two-dimensional fitting of Raman excitation maps in Ref. [58] (SI Section S7). The fit results for the *G*-band spectra with the highest intensity are shown with solid red lines in Figure 3c. The vertical dashed lines represent the fitted mode frequencies, namely 1566, 1573, 1576, 1583 and 1595 cm^{-1}.

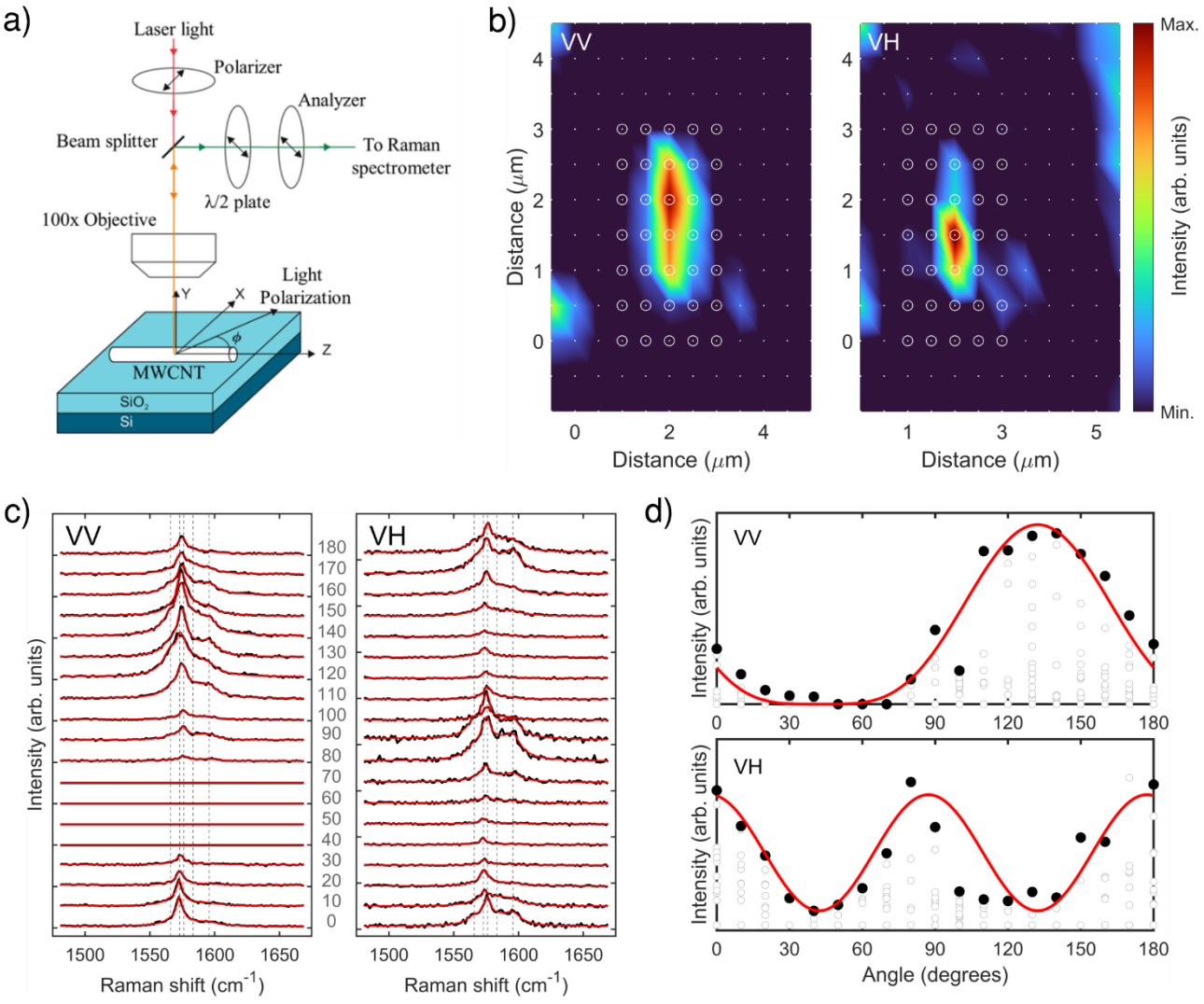

Figure 3. Polarization-dependent Raman response from structurally non-uniform MWCNTs (a) Schematic of the experimental set-up used for polarized Raman measurements on AD-MWCNTs. (b) *G*-band Raman maps in VV (left) and VH (right) configurations of a representative AD-MWCNT obtained by integrating the Raman intensities from 1510 to 1640 cm^{-1}. Small white dots indicate the RRS measurement coordinates. Open circles denote points used for Raman spectrum fitting. (c) Experimental and fitted Raman maps, showing *G*-band spectra of MWCNT as a function of the angle between the nanotube and the polarization of the incident light. d) The normalized integrated intensity of the *G*-mode with 1595 cm^{-1} for VV (top) and VH (bottom) configurations. Experimental data and

the fit with A_1 polarization dependence are shown as circles and solid red curves, respectively. The data points corresponding to the Raman spectra with the highest *G*-band intensity from (c) are highlighted with filled black circles.

We now show how the symmetry of Raman *G*-modes can be probed from the intensity dependence on the θ angle given the structural non-uniformity of a MWCNT. In general, the intensity of a polarized Raman signal is proportional to $|\hat{e}_i \cdot R \cdot \hat{e}_s|^2$, where $\hat{e}_i$ and $\hat{e}_s$ are the polarization of the incident and scattered photons, respectively, and R is the Raman tensor for a given mode[53]. We take as an example the *G*-mode with 1595 cm^{-1} (Figure 3c) and plot its fitted integrated intensities from all Raman spectra in the map as open circles in Figure 3d. The data points corresponding to the Raman spectra with the highest *G*-band intensity, *e.g.,* those shown in Figure 3c, are highlighted with filled black circles. We find that these VV and VH data points can be fitted simultaneously only by the A_1-symmetry function as shown in Figure 3d by the solid red line, which agrees well with the polarization behavior of *G*-modes in SWCNTs and MWCNTs with strong antenna effect[32,53]. We find that similar polarization dependences can be obtained for most of the shifted *G*-modes, given that they are sufficiently resolved in Raman spectra.

The presented polarized Raman mapping can be used to distinguish between structurally non-uniform (telescopic) MWCNTs and 1D moiré crystals based on collapsed SWCNTs[59]. Recently, a method for synthesizing such 1D moiré crystals was reported using an ultrasonication of AD-MWCNTs[59]. The collapsed SWCNTs and MWCNTs were in particular differentiated based on the different polarization dependence of the Raman modes since the polarization behavior of the former is no longer characterized by the antenna effect. Nevertheless, the authors of Ref. [59] probed only a few MWCNTs and did not report any structural irregularities along their length. This makes polarized Raman mapping a more systematic approach for such structural characterization.

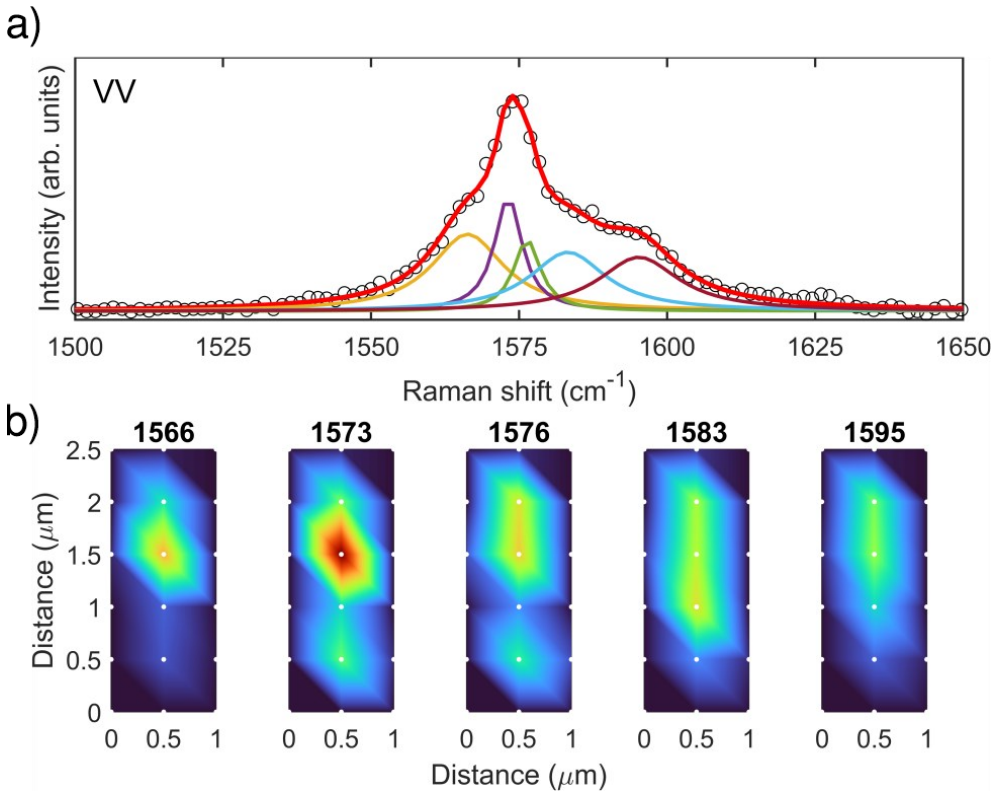

Figure 4. (a) Experimental *G*-band Raman spectrum (open dots) and the results of the fit (solid curves). Several *G*-modes with frequencies 1566, 1573, 1576, 1583 and 1595 cm^{-1} have been identified. (b) Distribution of the identified *G*-band intensities (peak height) from (a) along the MWCNT.

Finally, we analyze how integrated intensities corresponding to the individual shifted *G*-band components are distributed along the MWCNT. We take one VV spectrum of the MWCNT from Figure 3 as an example and provide its fit in Figure 4a. We then visualize the fitted intensity (peak height) distributions for each *G*-mode as a function of spatial coordinates in Figure 4b. In the first three maps (1566, 1573 and 1576 cm^{-1}), one can find zones of non-uniform Raman signal corresponding presumably to the structural changes in the MWCNT. Assuming the low-frequency *G*-band lines originate from the inner layers, these changes may be due to partial extraction of the layers during the sonication treatment (such extracted parts were observed in AFM and STM images

from the same batch of AD-MWCNT material in Ref. [23]). Besides, the variation in the Raman intensity can be due to the shift of the transition energy and the subsequent change in the resonance conditions for a particular layer, since electronic vdW coupling[6] is different in the extracted or covered parts. More detailed analysis of the maps in Figure 4b can be somewhat ambiguous due to the absence of HRTEM images exactly showing which regions of the MWCNT are empty or filled and the fact that Raman signal contains the information averaged over the large area on the MWCNT therefore both empty (extracted) and filled regions can contribute to the signal at one particular measurement location.

In principle, the presented approach for Raman imaging based on the shifted G-band can be used to probe other types of coaxial systems, such as one-dimensional (1D) vdW heterostructures, *i.e.*, coaxially-stacked carbon, boron nitride (BNNT) and molybdenum disulfide (MoS_2) nanotubes[60]. Their synthesis method is characterized by the layer-by-layer growth mechanism, which can lead to telescopic geometries if the growth is terminated too early. Moreover, such 1D vdW heterostructures are grown over the open holes or slits which allow combining optical and HRTEM measurements and therefore solving the problem of ambiguous data interpretation typical for substrate samples as described above. Finally, the carbon nanotubes in such 1D heterostructures are reported to have the shifted G-modes[60], which can be tentatively assigned to the effect of inter-layer mechanical vdW interactions studied in this work. Further experimental studies measuring G-mode shifts in multiple SWCNT@BNNT heteronatubes as a function of interlayer distance and diameter can verify these assignments.

CONCLUSIONS

In this work, we studied structurally non-uniformed AD-MWCNTs obtained through the ultrasonication process by combining polarized Raman imaging and spectroscopy and AFM. The

Raman imaging reveals the inhomogeneity of the Raman signal from AD-MWCNTs, which we argue is due to the inner layers extraction or damage during the sonication step of the dispersion procedure. We report the splitting of Raman-active *G*-band in isolated individual MWCNTs and interpret it in terms of the effect of inter-layer mechanical vdW coupling. Finally, we present a practical method for probing the polarization behaviour of MWCNTs with non-uniform Raman response based on Raman mapping and advanced data fitting allowing to identify the antenna effect.

Our work gives additional insights into the structural characterization of structurally non-uniform MWCNTs and, therefore, allows distinguishing between such MWCNTs and 1D moiré crystals based on collapsed SWCNTs[59] or studying telescopic 1D vdW heterostructures[60].

SUPPORTING INFORMATION

Supporting information is available at ... and includes (1) details of the deposition and on-chip purification of MWCNT samples, (2) AFM mapping of the individual AD-MWCNTs, (3) structural parameters of the investigated individual MWCNTs from AFM, (4) discussion of the absence of RBM in individual MWCNTs (5) details on the establishing *G*-band shift as a function of diameter, (6) list of G-mode frequencies in index-identified DWCNTs and a TWCNT (7) details on the fitting of individual Raman spectra.

AUTHOR INFORMATION

Corresponding author

*dmitry.levshov@uantwerpen.be, tel.: +32 3 265 24 79

Present Addresses

ǂ Physics Department, University of Antwerp, Universiteitsplein 1, B-2610 Antwerp, Belgium.

† School of Electrical Engineering and Automation, Aalto University, Espoo FI-00076, Finland.

Author Contributions

The manuscript was written through contributions of all authors. All authors have given approval to the final version of the manuscript.

ACKNOWLEDGMENTS

D.L acknowledges financial support from the Russian Foundation for Basic Research (Grant No. 18-29-19043 mk) and the postdoctoral grant (12ZP720N) of the Fund for Scientific Research Flanders (FWO). M.J.H acknowledges financial support from the University of Jyväskylä Graduate School.

REFERENCES

(1) Iijima, S. Helical Microtubules of Graphitic Carbon. *Nature* **1991**, *354*, 56–58.

(2) Leven, I.; Guerra, R.; Vanossi, A.; Tosatti, E.; Hod, O. Multiwalled Nanotube Faceting Unravelled. *Nat. Nanotechnol.* **2016**, *11*, 1082–1086.

(3) Amelinckx, S.; Bernaerts, D.; Zhang, X. B.; Van Tendeloo, G.; Van Landuyt, J. A Structure Model and Growth Mechanism for Multishell Carbon Nanotubes. *Science* **1995**, *267*, 1334–1338.

(4) Lehman, J. H.; Terrones, M.; Mansfield, E.; Hurst, K. E.; Meunier, V. Evaluating the Characteristics of Multiwall Carbon Nanotubes. *Carbon*, 2011, *49*, 2581–2602.

(5) Reich, S.; Thomsen, C.; Maultzsch, J. *Carbon Nanotubes: Basic Concepts and Physical Properties*; 1st ed.; WILEY-VCH Verlag GmbH & Co. KGaA, 2004.

(6) Liu, K.; Jin, C.; Hong, X.; Kim, J.; Zettl, A.; Wang, E.; Wang, F. Van Der Waals-Coupled Electronic States in Incommensurate Double-Walled Carbon Nanotubes. *Nat. Phys.* **2014**, *10*, 737–742.

(7) Koshino, M.; Moon, P.; Son, Y.-W. Incommensurate Double-Walled Carbon Nanotubes as One-Dimensional Moiré Crystals. *Phys. Rev. B* **2015**, *91*, 035405.

(8) Bonnet, R.; Lherbier, A.; Barraud, C.; Rocca, M. L. Della; Lafarge, P.; Charlier, J. Charge Transport through One-Dimensional Moiré Crystals. *Sci. Rep.* **2016**, *6*, 19701.

(9) Zhang, S.; Ma, Y.; Suresh, L.; Hao, A.; Bick, M.; Tan, S. C.; Chen, J. Carbon Nanotube Reinforced Strong Carbon Matrix Composites. *ACS Nano* **2020**, *14*, 9282–9319.

(10) Aoki, K.; Ogihara, N.; Tanaka, M.; Haniu, H.; Saito, N. Carbon Nanotube-Based Biomaterials for Orthopaedic Applications. *J. Mater. Chem. B* **2020**, *8*, 9227–9238.

(11) Chu, H.; Hu, X.; Wang, Z.; Mu, J.; Li, N.; Zhou, X.; Fang, S.; Haines, C. S.; Park, J. W.; Qin, S.; *et al.* Unipolar Stroke, Electroosmotic Pump Carbon Nanotube Yarn Muscles. *Science* **2021**, *371*, 494–498.

(12) Wu, Y.; Zhao, X.; Shang, Y.; Chang, S.; Dai, L.; Cao, A. Application-Driven Carbon Nanotube Functional Materials. *ACS Nano* **2021**, *15*, 7946–7974.

(13) Hoque, M. A.; Gil-Sepulcre, M.; de Aguirre, A.; Elemans, J. A. A. W.; Moonshiram, D.; Matheu, R.; Shi, Y.; Benet-Buchholz, J.; Sala, X.; Malfois, M.; *et al.* Water Oxidation Electrocatalysis Using Ruthenium Coordination Oligomers Adsorbed on Multiwalled Carbon Nanotubes. *Nat. Chem.* **2020**.

(14) Kang, S.; Jeong, Y. K.; Mhin, S.; Ryu, J. H.; Ali, G.; Lee, K.; Akbar, M.; Chung, K. Y.; Han, H.; Kim, K. M. Pulsed Laser Confinement of Single Atomic Catalysts on Carbon Nanotube Matrix for Enhanced Oxygen Evolution Reaction. *ACS Nano* **2021**, *15*, 4416–4428.

(15) Cabrillo, C.; Fernández-Perea, R.; Bermejo, F. J.; Chico, L.; Mondelli, C.; González, M. A.; Enciso, E.; Benito, A. M.; Maser, W. K. Formation of One-Dimensional Quantum Crystals of Molecular Deuterium inside Carbon Nanotubes. *Carbon* **2020**, *175*, 141–154.

(16) Sharma, K.; Costa, N. L.; Kim, Y. A.; Muramatsu, H.; Barbosa Neto, N. M.; Martins, L. G. P.; Kong, J.; Paschoal, A. R.; Araujo, P. T. Anharmonicity and Universal Response of Linear Carbon Chain Mechanical Properties under Hydrostatic Pressure. *Phys. Rev. Lett.* **2020**, *125*, 105501.

(17) Barnett, C. J.; Evans, C.; McCormack, J. E.; Gowenlock, C. E.; Dunstan, P.; Wade Adams; Orbaek White, A.; Barron, A. R. Experimental Measurement of Angular and Overlap Dependence of Conduction between Carbon Nanotubes of Identical Chirality and Diameter. *Nano Lett.* **2019**, *19*, 4861–4865.

(18) Tardani, F.; Sarti, S.; Sennato, S.; Leo, M.; Filetici, P.; Casciardi, S.; Schiavi, P. G.; Bordi,

F. Experimental Evidence of Single-Stranded DNA Adsorption on Multiwalled Carbon Nanotubes. *J. Phys. Chem. B* **2020**, *124*, 2514–2525.

(19) Lefebvre, J.; Finnie, P.; Fagan, J.; Zheng, M.; Hight Walker, A. R. Metrological Assessment of Single-Wall Carbon Nanotube Materials by Optical Methods. In *World Scientific Series on Carbon Nanoscience*; World Scientific Publishing Co. Pte Ltd, 2019; Vol. 9–10, pp. 45–104.

(20) Michel, T.; Levshov, D.; Zahab, A.-A.; Sauvajol, J.-L.; Paillet, M. Probing the Intrinsic Vibrational and Optical Properties of Individual Chirality-Identified Carbon Nanotubes by Raman Spectroscopy. In *Handbook of Carbon Nanomaterials Vol. 10: Optical Properties of Carbon Nanotubes*; Weisman, R. B.; Kono, J., Eds.; World Scientific Series on Carbon Nanoscience; World Scientific Publishing: Singapore, 2019; Vol. 10, pp. 75–112.

(21) Hokkanen, M. J.; Lautala, S.; Shao, D.; Turpeinen, T.; Koivistoinen, J.; Ahlskog, M. On-Chip Purification via Liquid Immersion of Arc-Discharge Synthesized Multiwalled Carbon Nanotubes. *Appl. Phys. A* **2016**, *122*, 634.

(22) Zhao, X.; Ando, Y.; Qin, L. C.; Kataura, H.; Maniwa, Y.; Saito, R. Multiple Splitting of G-Band Modes from Individual Multiwalled Carbon Nanotubes. *Appl. Phys. Lett.* **2002**, *81*, 2550–2552.

(23) Ahlskog, M.; Hokkanen, M. J.; Levshov, D.; Svensson, K.; Volodin, A.; van Haesendonck, C. Individual Arc-Discharge Synthesized Multiwalled Carbon Nanotubes Probed with Multiple Measurement Techniques. *J. Vac. Sci. Technol. B* **2020**, *38*, 042804.

(24) O'Connell, M. J.; Bachilo, S. M.; Huffman, C. B.; Moore, V. C.; Strano, M. S.; Haroz, E. H.; Rialon, K. L.; Boul, P. J.; Noon, W. H.; Kittrell, C.; *et al.* Band Gap Fluorescence from Individual Single-Walled Carbon Nanotubes. *Science* **2002**, *297*, 593–596.

(25) Miyata, Y.; Suzuki, M.; Fujihara, M.; Asada, Y.; Kitaura, R.; Shinohara, H. Solution-Phase Extraction of Ultrathin Inner Shells from Double-Wall Carbon Nanotubes. *ACS Nano* **2010**, *4*, 5807–5812.

(26) Erkens, M.; Cambré, S.; Flahaut, E.; Fossard, F.; Loiseau, A.; Wenseleers, W. Ultrasonication-Induced Extraction of Inner Shells from Double-Wall Carbon Nanotubes Characterized via in Situ Spectroscopy after Density Gradient Ultracentrifugation. *Carbon*

2021, *185*, 113–125.

(27) Bokova, S. N.; Obraztsova, E. D.; Grebenyukov, V. V.; Elumeeva, K. V.; Ishchenko, A. V.; Kuznetsov, V. L. Raman Diagnostics of Multi-Wall Carbon Nanotubes with a Small Wall Number. *Phys. Status Solidi Basic Res.* **2010**, *247*, 2827–2830.

(28) Nanot, S.; Millot, M.; Raquet, B.; Broto, J. M.; Magrez, A.; Gonzalez, J. Doping Dependence of the G-Band Raman Spectra of an Individual Multiwall Carbon Nanotube. *Phys. E Low-Dimensional Syst. Nanostructures* **2010**, *42*, 2466–2470.

(29) Wu, J.-B.; Lin, M.-L.; Cong, X.; Liu, H.-N.; Tan, P.-H. Raman Spectroscopy of Graphene-Based Materials and Its Applications in Related Devices. *Chem. Soc. Rev.* **2018**, *47*, 1822–1873.

(30) Telg, H.; Duque, J. G.; Staiger, M.; Tu, X.; Hennrich, F.; Kappes, M. M.; Zheng, M.; Maultzsch, J.; Thomsen, C.; Doorn, S. K. Chiral Index Dependence of the G+ and G- Raman Modes in Semiconducting Carbon Nanotubes. *ACS Nano* **2012**, *6*, 904–911.

(31) Avramenko, M. V.; Rochal, S. B.; Yuzyuk, Y. I. Symmetry of the Carbon Nanotube Modes and Their Origin from the Phonon Branches of Graphene. *Phys. Rev. B - Condens. Matter Mater. Phys.* **2013**, *87*, 035407.

(32) Duesberg, G. S.; Loa, I.; Burghard, M.; Syassen, K.; Roth, S. Polarized Raman Spectroscopy on Isolated Single-Wall Carbon Nanotubes. *Phys. Rev. Lett.* **2000**, *85*, 5436–5439.

(33) Levshov, D.; Michel, T.; Than, T.; Paillet, M.; Arenal, R.; Jourdain, V.; Yuzyuk, Y. I. I.; Sauvajol, J.-L. Comparative Raman Study of Individual Double-Walled Carbon Nanotubes and Single-Walled Carbon Nanotubes. *J. Nanoelectron. Optoelectron.* **2013**, *8*, 9–15.

(34) Levshov, D. I.; Tran, H. N.; Michel, T.; Cao, T. T.; Nguyen, V. C.; Arenal, R.; Popov, V. N.; Sauvajol, J.-L.; Zahab, A.-A.; Paillet, M. Interlayer Interaction Effects on the G Modes in Double-Walled Carbon Nanotubes With Different Electronic Configurations. *Phys. Status Solidi* **2017**, *254*, 1700251.

(35) Popov, V. N.; Levshov, D. I.; Sauvajol, J.-L.; Paillet, M. Computational Study of the Shift of the G Band of Double-Walled Carbon Nanotubes Due to Interlayer Interactions. *Phys. Rev. B* **2018**, *97*, 165417.

(36) Levshov, D. I.; Michel, T.; Arenal, R.; Tran, H. N.; Than, T. X.; Paillet, M.; Yuzyuk, Y. I.; Sauvajol, J.-L. Interlayer Dependence of G-Modes in Semiconducting Double-Walled Carbon Nanotubes. *J. Phys. Chem. C* **2015**, *119*, 23196–23202.

(37) Rochal, S.; Levshov, D.; Avramenko, M.; Arenal, R.; Cao, T. T.; Nguyen, V. C.; Sauvajol, J.-L.; Paillet, M. Chirality Manifestation in Elastic Coupling between the Layers of Double-Walled Carbon Nanotubes. *Nanoscale* **2019**, *11*, 16092–16102.

(38) Cambré, S.; Liu, M.; Levshov, D.; Otsuka, K.; Maruyama, S.; Xiang, R. Nanotube-Based 1D Heterostructures Coupled by van Der Waals Forces. *Small* **2021**, *2102585*, 1–26.

(39) Liu, Z.; Zhang, Q.; Qin, L.-C. C. Accurate Determination of Atomic Structure of Multiwalled Carbon Nanotubes by Nondestructive Nanobeam Electron Diffraction. *Appl. Phys. Lett.* **2005**, *86*, 191903.

(40) Deniz, H.; Derbakova, A.; Qin, L. C. A Systematic Procedure for Determining the Chiral Indices of Multi-Walled Carbon Nanotubes Using Electron Diffraction-Each and Every Shell. *Ultramicroscopy* **2010**, *111*, 66–72.

(41) Wen, Q.; Qian, W.; Nie, J.; Cao, A.; Ning, G.; Wang, Y.; Hu, L.; Zhang, Q.; Huang, J.; Wei, F. 100 Mm Long, Semiconducting Triple-Walled Carbon Nanotubes. *Adv. Mater.* **2010**, *22*, 1867–1871.

(42) Qin, L.-C. Determination of the Chiral Indices (n,m) of Carbon Nanotubes by Electron Diffraction. *Phys. Chem. Chem. Phys.* **2007**, *9*, 31–48.

(43) Liu, Z.; Qin, L. C. Breakdown of 2mm Symmetry in Electron Diffraction from Multiwalled Carbon Nanotubes. *Chem. Phys. Lett.* **2005**, *402*, 202–205.

(44) Kiang, C.-H.; Endo, M.; Ajayan, P.; Dresselhaus, G.; Dresselhaus, M. Size Effects in Carbon Nanotubes. *Phys. Rev. Lett.* **1998**, *81*, 1869–1872.

(45) Guo, W.; Guo, Y. Energy Optimum Chiralities of Multiwalled Carbon Nanotubes. *J. Am. Chem. Soc.* **2007**, *129*, 2730–2731.

(46) Nii, H.; Sumiyama, Y.; Nakagawa, H.; Kunishige, A. Influence of Diameter on the Raman Spectra of Multi-Walled Carbon Nanotubes. *Appl. Phys. Express* **2008**, *1*, 064005.

(47) Levshov, D. I.; Tran, H. N.; Paillet, M.; Arenal, R.; Than, X. T.; Zahab, A. A.; Yuzyuk, Y.

I.; Sauvajol, J.-L.; Michel, T. Accurate Determination of the Chiral Indices of Individual Carbon Nanotubes by Combining Electron Diffraction and Resonant Raman Spectroscopy. *Carbon* **2017**, *114*, 141–159.

(48) Farhat, H.; Son, H.; Samsonidze, G. G.; Reich, S.; Dresselhaus, M. S.; Kong, J. Phonon Softening in Individual Metallic Carbon Nanotubes Due to the Kohn Anomaly. *Phys. Rev. Lett.* **2007**, *99*, 145506.

(49) Gordeev, G.; Setaro, A.; Glaeske, M.; Jürgensen, S.; Reich, S. Doping in Covalently Functionalized Carbon Nanotubes: A Raman Scattering Study. *Phys. Status Solidi* **2016**, *253*, 2461–2467.

(50) Hatting, B.; Heeg, S.; Ataka, K.; Heberle, J.; Hennrich, F.; Kappes, M. M.; Krupke, R.; Reich, S. Fermi Energy Shift in Deposited Metallic Nanotubes: A Raman Scattering Study. *Phys. Rev. B* **2013**, *87*, 165442.

(51) Gaur, A.; Shim, M. Substrate-Enhanced O2 Adsorption and Complexity in the Raman G-Band Spectra of Individual Metallic Carbon Nanotubes. *Phys. Rev. B* **2008**, *78*, 125422.

(52) Cronin, S. B.; Swan, a. K.; Ünlü, M. S.; Goldberg, B. B.; Dresselhaus, M. S.; Tinkham, M. Measuring the Uniaxial Strain of Individual Single-Wall Carbon Nanotubes: Resonance Raman Spectra of Atomic-Force-Microscope Modified Single-Wall Nanotubes. *Phys. Rev. Lett.* **2004**, *93*, 167401.

(53) Zdrojek, M.; Judek, J.; Wasik, M. Laser Heating Control with Polarized Light in Isolated Multiwalled Carbon Nanotubes. *Phys. Rev. Lett.* **2012**, *108*, 1–5.

(54) Zólyomi, V.; Koltai, J.; Rusznyák, Á.; Kürti, J.; Gali, Á.; Simon, F.; Kuzmany, H.; Szabados, Á.; Surján, P. Intershell Interaction in Double Walled Carbon Nanotubes: Charge Transfer and Orbital Mixing. *Phys. Rev. B* **2008**, *77*, 245403.

(55) Artyukhov, V. I.; Gupta, S.; Kutana, A.; Yakobson, B. I. Flexoelectricity and Charge Separation in Carbon Nanotubes. *Nano Lett.* **2020**, acs.nanolett.9b05345.

(56) Steiner, M.; Freitag, M.; Tsang, J. C.; Perebeinos, V.; Bol, A. A.; Failla, A. V.; Avouris, P. How Does the Substrate Affect the Raman and Excited State Spectra of a Carbon Nanotube? *Appl. Phys. A* **2009**, *96*, 271–282.

(57) Iakoubovskii, K.; Minami, N.; Ueno, T.; Kazaoui, S.; Kataura, H. Optical Characterization of Double-Wall Carbon Nanotubes: Evidence for Inner Tube Shielding. *J. Phys. Chem. C* **2008**, *112*, 11194–11198.

(58) Wenseleers, W.; Cambré, S.; Čulin, J.; Bouwen, A.; Goovaerts, E. Effect of Water Filling on the Electronic and Vibrational Resonances of Carbon Nanotubes: Characterizing Tube Opening by Raman Spectroscopy. *Adv. Mater.* **2007**, *19*, 2274–2278.

(59) Picheau, E.; Impellizzeri, A.; Rybkovskiy, D.; Bayle, M.; Mevellec, J.-Y.; Hof, F.; Saadaoui, H.; Noé, L.; Torres Dias, A. C.; Duvail, J.-L.; *et al.* Intense Raman D Band without Disorder in Flattened Carbon Nanotubes. *ACS Nano* **2021**, *15*, 596–603.

(60) Xiang, R.; Inoue, T.; Zheng, Y.; Kumamoto, A.; Qian, Y.; Sato, Y.; Liu, M.; Tang, D.; Gokhale, D.; Guo, J.; *et al.* One-Dimensional van Der Waals Heterostructures. *Science* **2020**, *367*, 537–542.

TOC Graphic

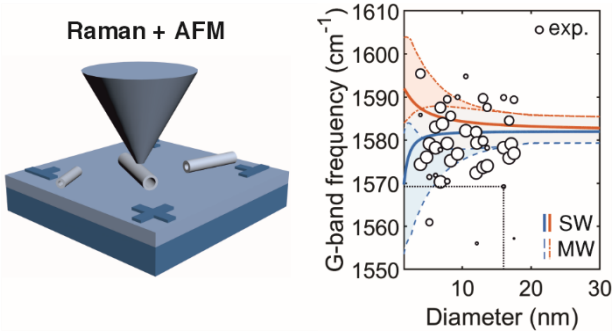
Raman + AFM
G-band frequency (cm-1)
1610
1600
1590
1580
1570
1560
1550
exp.
SW
MW
10
20
30
Diameter (nm)